*Solar-Terrestrial Physics. 2026, vol. 12, iss. 2, pp. 96–108. DOI: 10.12737/stp-122202611. © 2026 V.V. Oreshko, S.A. Tyul'bashev Published by INFRA-M Academic Publishing House*

DOI: 10.12737/stp-122202611
EDN: DPGQIR

Received November 17, 2025
Accepted February 18, 2026

# RADIO TELESCOPE FOR MONITORING THE STATE OF INTERPLANETARY PLASMA

**V.V. Oreshko**
*Lebedev Physical Institute RAS,*
*Astro Space Center,*
*Pushchino Radio Astronomy Observatory,*
*Pushchino, Russia, oreshko@prao.ru*

**S.A. Tyul'bashev**
*Lebedev Physical Institute RAS,*
*Astro Space Center,*
*Pushchino Radio Astronomy Observatory,*
*Pushchino, Russia, serg@prao.ru*

**Abstract.** This paper examines scientific and technical requirements for a specialized radio telescope which allows us to make a space weather forecast from observations of radio sources that scintillate on moving irregularities of interplanetary plasma. It is shown that in addition to forecasting the radio telescope can solve other scientific problems. A variant of the antenna's technical implementation is proposed, and the structure of the radio telescope is studied. The radio telescope is a spaced antenna array consisting of modules, each with 16 (4×4) base antenna elements representing 2 orthogonal dipoles. The effective area of a module is 16 $m^2$ at the central frequency of 180 MHz; the total operating frequency band is 120–240 MHz. The module's field of view is at least 400 sq.deg. in the range ±50° from the zenith at the central frequency. The sensitivity drops by a factor of 2 at the edges of the field of view. It is demonstrated that the telescope consisting of 64 modules will provide a forecast at least 2–3 times a day. The estimated accuracy of predicting the arrival time of coronal mass ejection at Earth is one hour.

**Keywords:** space weather, interplanetary scintillation, forecast, low-frequency observations, Large Phased Array (LPA).

## INTRODUCTION

Interplanetary scintillation of compact radio sources was discovered by Hewish in 1964 [Hewish et al., 1964]. Two years later, the solar wind speed was estimated from observations of interplanetary scintillation on spaced antennas [Hewish et al., 1966]. In 1974, coronal mass ejections (CMEs) were identified [Gosling et al., 1974], and in 1976 their propagation speeds were measured [Gosling et al., 1976; Vlasov et al., 1979]. In 1979, two-dimensional maps of distribution of the level of interplanetary scintillation were drawn which showed CME propagation from the Sun [Vlasov et al., 1979]. It is obvious that solar flares lead to changes in the solar wind, and geomagnetic storms are caused by the arrival of flare plasma ejections at Earth (see, e.g., [Wagner, 1982]).

The charged particle flux coming from the Sun can produce various geomagnetic effects: affect low-orbit spacecraft (SC) (heating of the atmosphere results in an increase in its size, and SC experience deceleration in the atmosphere); influence radio wave propagation (the ionosphere is excited, giving rise to interference); trigger geomagnetically induced currents in long circuits (transformers may be overloaded due to power supply failure), etc. (see, e.g., [Petrukovich, 2008]). These examples emphasize the importance of space weather forecasting.

There are several large centers in the world for which forecasting geomagnetic activity is one of the main tasks. In Russia, such centers are located, for example, in IZMIRAN [http://spaceweather.izmiran.ru/], IPG [http://ipg.geospace.ru/space-weather-forecast.html], ISTP [https://iszf.irk.ru/megascience/]. The foreign centers which are worth mentioning are NOAA (USA) [www.swpc.noaa.gov ], WDC (Japan) [wdc.kugi.kyoto-u.ac.jp], ESA (Europe) [https://swe.ssa.esa.int /], CESSI (India) [http://www.cessi.in/spaceweather /], NSSC (China) [http://www.spaceweather.org/ISES/rwc/rwc_cn_a.html].

If we consider the activity of these centers, we can find common details in space weather forecasting. Long-term, medium-term, and short-term forecasts have different observational frame. For example, we observe a powerful solar flare followed by CME, which is associated with a large sunspot or group of sunspots; therefore, after a solar rotation (27–28 days) we may see the flare again. The forecasting is probabilistic and is related to the fact that large sunspots or groups of sunspots are long-lived objects and their lifetime is longer than one solar rotation. Another type of geoeffective large-scale disturbances — coronal hole-associated corotating interaction regions between variable-speed streams — can also be predicted from the 27-day recurrence. This is how a long-term forecast is made.

If sunspots are observed on the limb, in case of a flare (the assumption based on the flare statistics) we can expect that in 8–12 days we will feel it on Earth. This is a medium-term forecast.

If there are powerful solar flares a day or two before or during the passage of an active region through the central meridian, they can lead to a CME that reaches Earth. From observations of the solar surface and corona, the probable speed of CME and its intensity are calculated (see, e.g., [Millward et al., 2013; https://ccmc.gsfc.nasa.gov/models/WSA-Enlil-at-SWPC~3/]). This is a short-term forecast.

The pattern presented above is very incomplete and slightly exaggerated. The main thing in this pattern is that space weather forecasting, despite daily observations of the Sun and its corona from radio ranges to X-rays, includes an element of unpredictability. Sunspots may not produce a flare accompanied by CME, they may disappear during a solar rotation, may produce a flare a few days before or a few days after passing through the central meridian, and therefore the ejection may pass by Earth.

Observations by GOES, ACE, DSCOVR, and Wind SC, located at the Lagrange point L1, provide very high forecast accuracy [https://www.ncei.noaa.gov/; https://www.nesdis.noaa.gov/current-satellite-missions/currently-flying/dscovr-deep-space-climate-observatory; https://www.swpc.noaa.gov/products/ace-real-time-solar-wind]. This point is situated on the Sun—Earth line at a distance of 1.5 million km from Earth. The instruments installed in GOES, Wind, ACE, and other SC can measure the direction of the magnetic field, which is crucial for forecasting (i.e., after the measurement, it becomes clear whether magnetic field lines will reconnect and whether there will be a geomagnetic storm), as well as estimate the speed and concentration of charged particles passing through SC. The CME propagation speed can be from several hundred to thousands of kilometers per second. It is easy to estimate that at a propagation speed of 1000 km/s CME will reach Earth in less than half an hour after passing through L1. Owing to the response time of services, there is practically no time to prepare for the arrival of CME at Earth.

Thus, the standard forecasting algorithm includes the following steps: we observe the Sun and the corona, monitor flares; when observing strong class M and X flares in X-rays, we specify the initial velocity of charged particles, the magnetic field strength, and the particle density and calculate the expected time of arrival of an ejection at Earth; on SC at L1, we record the actual arrival of CME. That is, in the first step, the Sun and its corona are observed; in the next step, the arrival of CME at L1 is monitored and its parameters are determined.

There are no observations of ejections between the Sun and Earth in this scheme, although it was shown more than 45 years ago that the interplanetary scintillation method can measure the CME propagation speed at distances from fractions of the astronomical unit up to Earth's orbit [Vlasov, 1979]. At first glance, it seems inexplicable that the stages of CME recording and estimation of its propagation speed at intermediate distances between the Sun and Earth are omitted from the forecasting procedure. Looking ahead, let us say that this is due to the fact that observations of scintillating radio sources require radio telescopes which have high sensitivity and can make daily observations during the daytime.

The interplanetary scintillation method is generally used to study flares post factum (see, e.g., [Bisi et al., 2010] and references therein). In a routine study, it is assumed that for each scintillating source there is a dependence of the scintillation index on elongation (the angle between directions to the source and to the Sun when observed from Earth), derived from earlier observations of the radio source. Then, observing a scintillating source today, we compare its scintillation index $m$ with the average scintillation index of the same source $m_{\text{av}}$, obtained earlier for the same elongation. This so-called $g$ index ($g=m/m_{\text{av}}$) provided a basis for CME research. Nonetheless, as shown in [Chashei et al., 2019; Lukmanov et al., 2022], considerable differences in the annual and monthly average dependence of the scintillation index on elongation are observed each year, and this dependence cannot be used for daily forecasting.

When forecasting from observations with the Large Phased Array of the Lebedev Physical Institute (LPI LPA), it was decided to employ scintillation indices for adjacent dates [Shishov et al., 2016]. The current scintillation index is divided by the scintillation index for the previous day, and in the case of a sharp change in the index 1.5 or more times, it is assumed that the ejection is on the line of sight. As an example, here is a fragment of a Figure from [Shishov et al., 2016], where scintillation enhancement around the Sun in the form of a ring structure is clearly visible (Figure 1). Part of this structure falls within declinations below –9°, i.e. within a region without LPA beams. We drew rings in Figure 1. The distance between the inner and outer fronts is less than 30° at elongations, or 0.3 AU.

From observations of scintillating radio sources, we can record an ejection [Kojima et al., 1998; Manoharan et al., 2001; Shishov et al., 2016; Fallows et al., 2023; Morgan et al., 2023], estimate its propagation speed in various ways (e.g., [Tokumaru et al., 2012; Glubokova et al., 2013; Mejia-Ambriz et al., 2015; Iwai et al., 2019]), see the symmetry or asymmetry of CME propagation relative to the central meridian, predict the time of arrival of corotating structures at Earth [Tokumaru et al., 2010; Mejia-Ambriz et al., 2015; Romero-Hernandez et al., 2015]. Almost all of the above works were carried out using meridian instruments, which perform observations of scintillating radio sources once a day. In the absence of observations for the next day, a forecast cannot be made, since scintillation of radio sources for two consecutive days is compared. The second problem is that for forecasting it is necessary to observe

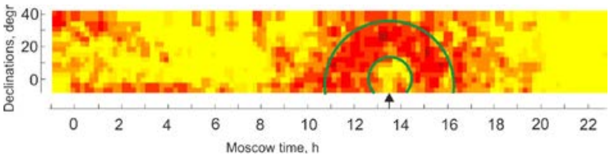

*Figure 1*. CME recorded on April 8, 2014. The Sun is located inside the yellow zone indicated by the arrow on the horizontal scale. A fragment of a ring is seen around the Sun, inside of which there is a sharp (twofold or more) increase in the scintillation index. Color shades from yellow to purple show variations in the scintillation index of sources from 0.2 to >1.5 between April 7 and 8. We took the Figure from [Shishov et al., 2016] and partially changed it

many dozens, and preferably hundreds, of compact radio sources. If an instrument has only one antenna pattern (one beam), observing hundreds of sources a day will span the entire daytime of the radio telescope, even with its outstanding sensitivity.

The only instrument that can provide a regular space weather forecast from observations of interplanetary scintillation is LPI LPA [Shishov et al., 2016]. Four-year forecasting experience [https://sw.prao.ru/] suggests that meridian instruments have fundamental limitations that do not allow us to make a forecast in some cases. For example, for LPA (reception at a wavelength of 2.7 m), scintillation changes should be observed at elongations ~25°–60° (corresponds to distances 0.4–0.85 AU). At a propagation speed of 1500 km/s (fast CME), an ejection will cover this distance for 12 hrs. If CME propagates at night, it will be omitted.

Note also that researchers using observations of scintillating radio sources to study interplanetary plasma and individual CMEs have attempted to organize an informal community of observers from Mexico, India, Russia, Japan, the USA, Australia, Korea, and other countries [Bisi et al., 2017].

Along with meridian instruments, during test observations of scintillating radio sources, scintillation variations during CME passage were recorded by the Murchison Widefield Array (MWA) [Waszewski et al., 2023]. The distinct possibility of recording CME by such a system has been demonstrated. The maps show the width of the propagating CME front (approximately 0.1–0.15 AU). The same median values of the CME front width (0.1–0.15 AU) are given in [Ghuge et al., 2025] after analyzing 152 CMEs.

The main advantage of aperture synthesis systems in space weather forecasting is the ability to track CMEs by switching over the antenna pattern in both right ascension and declination. The main disadvantage of such systems is the long processing time when drawing maps, i.e. CMEs will be detected only during postprocessing. For meridian instruments, the processing of observations can actually be done in real time, since the delay is related only to waiting for the source to be recorded as it passes through the meridian, and the processing itself occurs almost instantly.

In this paper, we explore the possibility of developing a specialized instrument that will allow us to make and process observations in near real time.

## REQUIREMENTS FOR THE NEW RADIO TELESCOPE

To develop a special-purpose radio telescope that can provide space weather forecasts in near real time, it is necessary to answer two main questions as to what sensitivity the instrument should ensure and how many scintillating radio sources need to be observed to make a forecast.

Obviously, the new telescope should realize an aperture synthesis system that will allow us, after the initial detection of an ejection, to monitor it along the entire front, switching over the central beam in both right ascension and declination. To reduce the processing time, it is essential that beams directed at preselected scintillating radio sources are formed in the area from which the map is synthesized. In this case, the map obtained by the aperture synthesis method is unrequired.

From an observer's point of view, interplanetary scintillation is a random change in the emission flux density (intensity) with a characteristic time scale from fractions of a second to one second. Daily measurements of the fluctuating flux from sources show that at an elongation in the source scintillation index there is first a maximum and then a gradual decrease. The maximum value depends on angular dimensions of the source and reaches 1 for a point source, and at large elongations it runs to ~0.1, i.e. the maximum difference in the scintillation index can be one order of magnitude [Readhead, 1971; Marians, 1975; Manoharan et al., 1995]. If a source is not point, the maximum scintillation index is less than 1 and the difference between the maximum and minimum of the index will be smaller. The scintillation index $m$ is defined as follows: $m^2 = \left\langle \left(I - \langle I \rangle\right)^2 \right\rangle \Big/ \langle I \rangle^2$, where $I$ is the observed value of the current intensity. Thus, no matter how strong CME is, scintillation index changes will always be less than one order of magnitude. In practice, these changes amount to 2–6 times, since compact radio sources are usually not point and at the best elongations their scintillation index is noticeably less than 1.

The typical depth of the CME front, as indicated above, is 0.1–0.15 AU, or 9°–14°. To reliably detect it (tracking the front in depth), we must record several sources located in the region which the CME has not yet reached, in the region of the ejection, and in the region that it has already passed. Thus, there should be at least 2–3 compact sources in the depth of the CME front, which the radio telescope must track. Hence, if we proceed only from the depth of the front, the radio telescope should make observations of sources with a density of at least one source per 3–5 sq. deg.

According to observations, the width of the CME front varies very widely, from 2° to 360° in the sky plane (see, e.g., [Wang et al., 1998; Yashiro et al., 2004; Chen, 2011]). The apparent problem is that we can skip a narrow ejection, since we have to see scintillating sources on the line of sight, and for a narrow ejection going toward us elongations can fall within ε<25°, where the degree of interplanetary scintillation in the meter range drops sharply. However, no matter how narrow the ejection may be, when approaching Earth at some moment it will occupy the entire field of view of the radio telescope, i.e. we will see it at all elongations. We can calculate the distances from the Sun at which we have time to predict CME of any width. So, for an ejection 2° wide, this distance will be less than 1.5 million km from Earth, and this means that such an ejection will first be detected at L1. In this case, our forecast will be useless. Calculations show that to detect an ejection, its minimum width should be 20°. In this case, we manage to detect the ejection at approximately 0.9 AU from the Sun (0.1 AU to Earth). At a CME speed of 1000 km/s (0.1 AU), the ejection front will reach Earth in 4 hrs, and there will be time for repeated observation allowing us to estimate the propagation speed of the ejection.

Fortunately, the total number of narrow CMEs is relatively small. According to [Yashiro et al., 2004], narrow (front width ≤20°) CMEs observed in white light ranged from 11 to 23 % (16 % median value) during the period 1996–2002. At the same time, even with a slight deviation from the Sun—Earth line, the ejection can pass by Earth or touch it tangentially without causing significant changes in the magnetosphere.

From the depth of the ejection front and its minimum width, we obtain a 20°×10° region, which, looking ahead, is half the area covered by the antenna pattern of the module consisting of 4×4 antenna elements. To accurately estimate the speed of the front, we should observe sources ahead of the front, in the CME front, and after it. We suppose that for reliable forecasting it is necessary to have uniform coverage of the sources with the antenna pattern of the module and 6–7 scintillating radio sources in the CME region before, during, and after its passage. Then, at least 20 sources should fall within the module's field of view and the required minimum source density should be one source per 20 sq. deg.

According to [Artyukh et al., 1998], due to searching for scintillating radio sources at a frequency of 102.5 MHz in an area of size 300 sq. deg. 144 scintillating sources with flux density fluctuations $\Delta S \geq 0.4$ Jy have been found. This corresponds to a density of 1 source per 2 sq. deg. Assume the minimum level of source flux density fluctuations to be $\Delta S = 0.4$ Jy at 102.5 MHz. In actual observations, this level of $\Delta S$ is not redundant, since the recorded value of $\Delta S$ decreases with increasing elongation, and estimated $\Delta S$ from [Artyukh et al., 1998] refers to observations at the best available elongations. Thus, in practice, we should be able to estimate the scintillation index for sources 2–6 times weaker.

First of all, it is necessary to determine the operating frequency range at which it is planned to observe scintillating sources. The maximum scintillation of compact (less than 1") sources in the interplanetary plasma falls within the meter radio wave range; in this case, the higher the frequency, the lower the elongations at which observations can be performed. In the low-frequency part of the 30–70 MHz meter range, sky noise is very high (high galactic background temperature), which reduces sensitivity, as well as there may be a disturbing effect of Earth's ionosphere, leading to intense ionospheric scintillation of sources and a visible shift in their coordinates. Furthermore, the 87–108 MHz range is occupied by broadcasting stations. The 240–290 MHz frequency band is almost completely occupied by radio navigation stations and space—ground telemetry. The frequency range 120–240 MHz is, therefore, optimum for monitoring the interplanetary plasma by a radio telescope in the meter range.

From the minimum level of flux fluctuations $\Delta S = 0.4$ Jy at 102.5 MHz, we can determine the required sensitivity of the radio telescope at the average frequency of 180 MHz of the new antenna's range. With an assumed spectral index $\alpha=0.7$ ($S \sim \nu^{-\alpha}$) for extragalactic compact radio sources, the threshold flux density decreases to $\Delta S=0.26$ Jy. In view of the decreased sensitivity when the beam deviates from the normal to the plane of the phased antenna array (PAA) 4 times for elevation angles of 30° or wider, to confidently monitor changes in the scintillation index at different elongations, the threshold sensitivity of the radio telescope should provide a signal-to-noise ratio ($S/N$) of at least 50 for a source observed at the zenith. Then, under the best observation conditions, we can use sources with flux density fluctuations 0.26/4=0.065 Jy at $S/N=12$. Artyukh, Tyul'bashev [1996a, b] show that at such values of $S/N$ it is possible to effectively work with scintillating radio sources. By determining the sensitivity of the total power radiometer for the radio telescope, we can find the required effective antenna area for a given frequency band and signal accumulation time by the following formula: $A_{\text{eff}} = \dfrac{2kT_{\text{sys}}\dfrac{S}{N}}{\Delta S\sqrt{n\Delta\nu\tau}}$, where $S/N=50$, $k$ is the Boltzmann constant; $T_{\text{sys}}$ is the system temperature; $\Delta S$ is the minimum level of fluctuations in the source flux; $\tau$ is the signal accumulation time; $\Delta\nu$ is the receiving frequency band; $n$ is the number of polarizations.

The system temperature is defined as the galactic background temperature plus the receiver temperature. According to [Turtle, Baldwin, 1962], the background temperature at a frequency of 178 MHz varies from 120 K outside the galactic plane to more than 2000 K in the galactic plane. However, the region of high temperatures occupies a narrow band in the sky plane (less than ±10° of the galactic plane), and outside the galactic plane the background temperature of 200 K at a frequency of 180 MHz can be taken for estimates. Suppose that a receiver temperature is 100 K, we get $T_{\text{sys}}=300$ K outside the galactic plane.

With a signal accumulation time of 15 min, a receiving band of 15 MHz, and signal reception in two polarizations, the estimated effective antenna area should be at least 970 m$^2$.

## CHARACTERISTICS OF THE BASE ANTENNA ELEMENT AND MODULE

Currently, two new-generation radio telescopes are known to actively operate at low frequencies (meter range): the LOw-Frequency ARray (LOFAR) [van Haarlem et al., 2013] and the Murchison Widefield Array (MWA) [Tingay et al., 2013]. LOFAR has two antenna systems: low-frequency (30–80 MHz) and high-frequency (120–240 MHz). MWA operates in the 80–300 MHz range. Both radio telescopes use a broadband dipole as the antenna element of the phased array.

Characteristics of the PAA element define the operating frequency range, the field of view of the radio telescope antenna as a whole, as well as the required number of elements for a given effective area of the radio telescope antenna. We have selected the operating frequency range of the radio telescope from 120 to 240 MHz, and the antenna element should ensure efficient operation in this frequency range. The range of angles of deviation of the antenna beam from the normal to the plane of the antenna array (field of view) is also determined by the beam pattern of the antenna element, and its gain (effective area) directly depends on the antenna pattern: the narrower the pattern, the higher the antenna gain. For a broadband antenna, its beamwidth and gain depend on frequency. Matching the antenna to the load, which determines how much of the received signal power is transmitted to the load, is also frequency dependent and is an essential parameter of a broadband antenna.

Note also that antenna arrays employ unidirectional antenna elements, i.e. shielded transmitters. The total radiation field is formed by the antenna field and the reflected field, the distance between the antenna and the shield defines the direction of the maximum radiation peak. In the direction perpendicular to the plane of the shield, the maximum radiation will be at a distance of 0.25λ (λ is the wavelength) between the shield and the antenna, since the antenna field and the reflected field are in phase. Due to the fact that the wavelength in the operating frequency range varies from 1.25 to 2.5 m, the distance from the antenna to the shield is optimized for the 180 MHz central frequency of the range. The distance between the shield and the transmitter also affects the antenna beamwidth and gain, the frequency characteristics of the antenna, and its matching to the load.

As a base antenna element, we can utilize various versions of broadband dipoles, as in LOFAR and MWA, or broadband closed-loop antennas, as in the prototype of a VNF radio telescope with a wide field of view [Dagkesamanskii et al., 2020]. In order to select an optimal antenna element for the proposed telescope, we have examined two antenna elements: a bowtieTriangular dipole (bowtie dipole) and a triangular closed-loop antenna (delta antenna). We have carried out model calculations of antenna parameters and experimental studies of prototypes of antenna elements.

Let us list the works that were done, without going into further details. For the antenna element, the following factors were considered: continuous or discontinuous filling of the dipole; thickness of conductive elements; load point; load resistance; central receiving frequency; impedance level; antenna resistance dependence on frequency; balun transformation ratio; obtained field of view. As a result, we obtained optimal matching throughout the operating frequency range for both antenna elements being tested. The elements were modeled using the MMANA-GAL software [Goncharenko, 2002], as well as the Antenna Toolbox package [https://www.mathworks.com/products/antenna.html] for the Matlab programming environment. Figure 2 presents prototypes of the antenna elements under study with a 2.5×2.5 m shield, which were built using the results of modeling of antenna elements.

Measurements of characteristics of the prototypes of the antenna elements confirmed the calculated parameters of the bowtie dipole and the delta antenna. For the proposed radio telescope, the bowtie broadband dipole turned out to be preferable to the delta antenna, since it has a wider field of view and a better antenna matching to the load in the 120–240 MHz frequency range.

Thus, a version of the broadband dipole with the shield optimized for a frequency of 180 MHz has been developed. Figure 3 depicts the antenna pattern of the dipole at a frequency of 180 MHz in the angle range 0°–180° from the shield plane. The half–power antenna beamwidth (in Figure 3, sector C1–C2, highlighted in color) is 98°, which is close to the required ±50°.

At a frequency of 150 MHz, the antenna beamwidth is 90°; and at a frequency of 210 MHz, 108°. The effective area of the dipole drops from 3 m$^2$ at a frequency of 120 MHz to 0.7 m$^2$ at a frequency of 240 MHz. The efficiency of the antenna is also affected by its mismatching to the load. For the developed antenna element, the power-loss ratio due to the mismatching to the load decreases with increasing frequency: 50 % at 120 MHz and 8 % at 240 MHz. In view of the antenna mismatching, the effective dipole area is 1.5–0.65 m$^2$ in the

*Figure 2*. Antenna elements "bowtie" (left) and "delta" (right) on a test bench

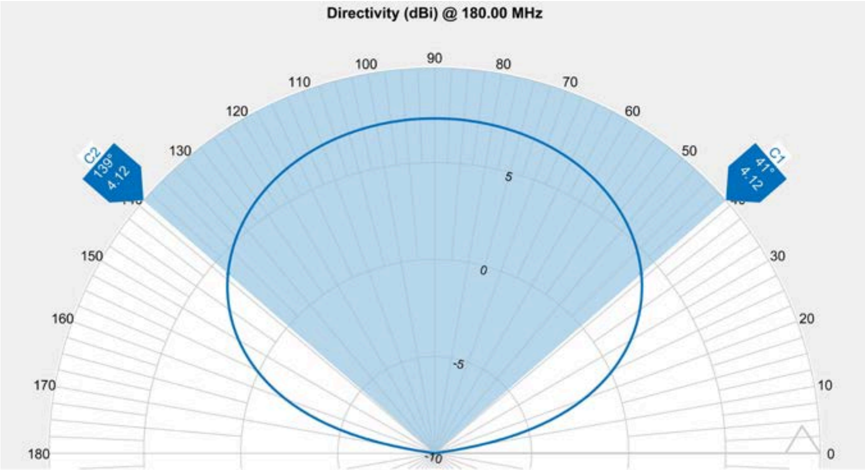

*Figure 3*. Antenna pattern of a shielded dipole at a frequency of 180 MHz in the hemisphere. Numerals along the radius indicate the signal amplitude (in dBi) relative to an isotropic transmitter

operating frequency range, approximately 1.1 m$^2$ in the middle of the range. To form an effective antenna area of 1000 m$^2$, it is necessary to have about 1000 broadband dipoles in LPA.

A large number of LPA elements in correlation processing of signals from each element require great performance of the correlator and a wide variety of analog-to-digital converters with digital signal preprocessing.

To reduce the amount of calculations, in LOFAR (high-frequency part) and MWA radio telescopes some of the elements are phased in an analog way, using controlled delay lines to form an antenna module of 16 elements (antenna array of 4×4 base antenna elements).

This variant is also suitable for the proposed radio telescope. The 4×4 antenna module has an antenna beamwidth ~20°±5°, depending on frequency and array configuration. As a result, the visible area in the sky will be 300 or more sq. deg., which, as shown above, allows us to simultaneously monitor more than 100 compact (scintillating) sources.

To estimate parameters of the 4×4 antenna module, calculations have been made for various distances (array spacing) between the module's elements. As is known, the beam uniqueness condition (diffraction maximum) of the antenna array within actual antenna angles is the requirement for the distance between array elements, which should not exceed half the wavelength at the operating frequency of the antenna [Voskresenskii, 1981]. In our case, the distance between elements of the antenna array at the lower frequency of the range should be no more than 1.25 m; at the upper frequency, no more than 0.625 m. As you can see, in such a wide frequency range we cannot ensure the absence of additional antenna array beams, since in the upper part of the frequency range the distance between elements must be less than their geometric dimensions. Moreover, the closer the antenna elements are located to each other, the greater their mutual influence, which distorts their characteristics. Calculations of antenna module parameters for rectangular array spacing $d$=1.2, 1.1, and 1 m are presented in Table.

Calculations were performed for frequencies of 150, 180, and 210 MHz, and power losses due to dipole mismatching are shown for loads of 300 and 200 ohm. The dipole matching to the load was calculated with regard to the mutual influence of elements in the array; Table lists average values for 16 dipoles. Table shows the sector of zenith angles (the array is installed horizontally), in which the amplitude of the main beam harmonic of the antenna

Output parameters of the antenna module for different frequencies

| Parameter | 150 MHz | | | 180 MHz | | | 210 MHz | | |
|---|---|---|---|---|---|---|---|---|---|
| | $d$=1.2 | $d$=1.1 | $d$=1.0 | $d$=1.2 | $d$=1.1 | $d$=1.0 | $d$=1.2 | $d$=1.1 | $d$=1.0 |
| Beamwidth (deg.) | 24 | 25 | 28 | 20 | 22 | 24 | 16 | 18 | 20 |
| Effective area (m$^2$) | 24 | 21 | 17.6 | 22 | 19.2 | 16.5 | 19.5 | 18.2 | 15.4 |
| Field of view — beam cross-section area (sq. deg.) | 528 | 576 | 728 | 360 | 440 | 528 | 256 | 324 | 400 |
| Zenith angle at beam harmonic level ≤ side lobes (deg.) | ±33 | ±45 | ±57 | ±15 | ±25 | ±32 | 0 | ±10 | ±17 |
| Power loss due to dipole mismatching (mean value, %):<br>at a load of 300 ohm | 21 | 20 | 14 | 13 | 10.5 | 6 | 11 | 7 | 3.4 |
| at a load of 200 ohm | – | 14.5 | – | – | 13 | – | – | 15 | – |

pattern is lower than the level of the side lobe of the antenna array. According to the selected effective area, field of view, and antenna matching, the preferred array spacing *d*=1.1 m for the 4×4 antenna module.

Figure 4 illustrates the calculated beam pattern of the antenna module with the 1.1 m array spacing at 180 MHz. The beams illustrated in Figure 4 correspond to the directions formed by the phasing system with a delay step $\Delta t$=0.5*n* ns, where *n* are integers from 0 to 7. The beam in the zenith direction (phase delay is 0) is highlighted in red, with half-power beamwidth (C1–C2) indicated.

It is apparent that when the beam deviates from the normal to the array plane by 45° or more, the principal beam harmonic of the array exceeds its amplitude. There is an ambiguity in determining the location of sources in the sky. However, during observations with source signal accumulation (source tracking) in full LPA, the speed of apparent motion of the sources for different declinations will vary and the signal will be accumulated only for the observed source, which solves the problem of ambiguity.

The radio telescope sensitivity, among other parameters, is determined by the intrinsic noise of the receiving system. To minimize noise and eliminate signal losses in a transmission path from an antenna to a receiver input, a signal amplifier should be mounted directly on the antenna. With minimum intrinsic noise, this antenna amplifier should have a gain sufficient for subsequent RF path elements to not increase the receiver noise. When calculating the sensitivity of the radio telescope, it was assumed that the noise of the receiving system does not exceed 100 K, hence the intrinsic noise of the antenna amplifier should not exceed this value. At present, the element base of radio electronics makes it possible to apply an antenna amplifier with such parameters without high costs. We have developed an antenna amplifier with 70 K intrinsic noise and 22 dB gain in the operating frequency range. This amplifier was used for modeling the 4×4 antenna module.

For experimental verification, a prototype of the 4×4 antenna module was developed from a broadband bow-tie dipole with a shield, a low-noise antenna amplifier, and a controlled phasing system with a delay step of 0.5 ns in the range from 0 to 15.5 ns.

## Antenna module

### *Realization*

The antenna module was developed around base antenna elements arranged in the north-south/west-east directions in the 4×4 format with 1.1 m spacing between the elements. The 4×4 antenna module prototype is illustrated in Figure 5. To receive a signal in two polarizations, dipoles of each polarization are structurally combined into one element with their orthogonal orientation. Antenna amplifiers are mounted directly on the

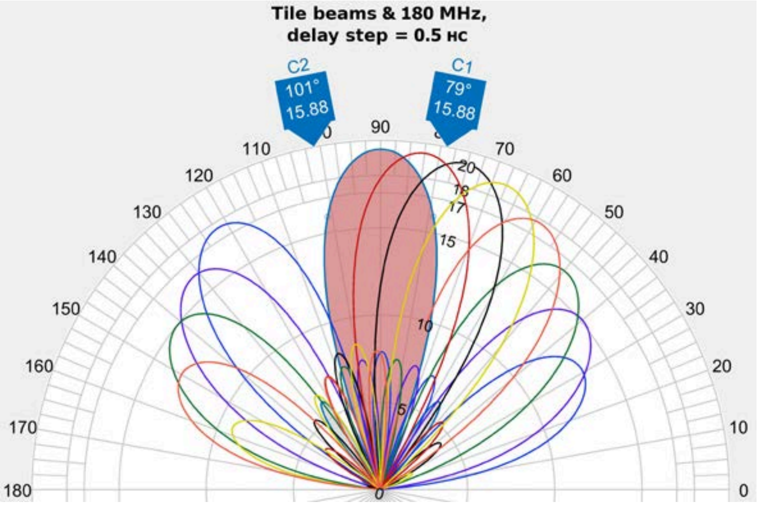

*Figure 4*. Calculated positions of antenna module beams with a delay step $\Delta t$=0.5*n* ns in the hemisphere. The gain of the antenna module is denoted by numerals (in dBi) along the radius relative to an isotropic transmitter

*Figure 5*. Prototype of the 4×4 antenna module

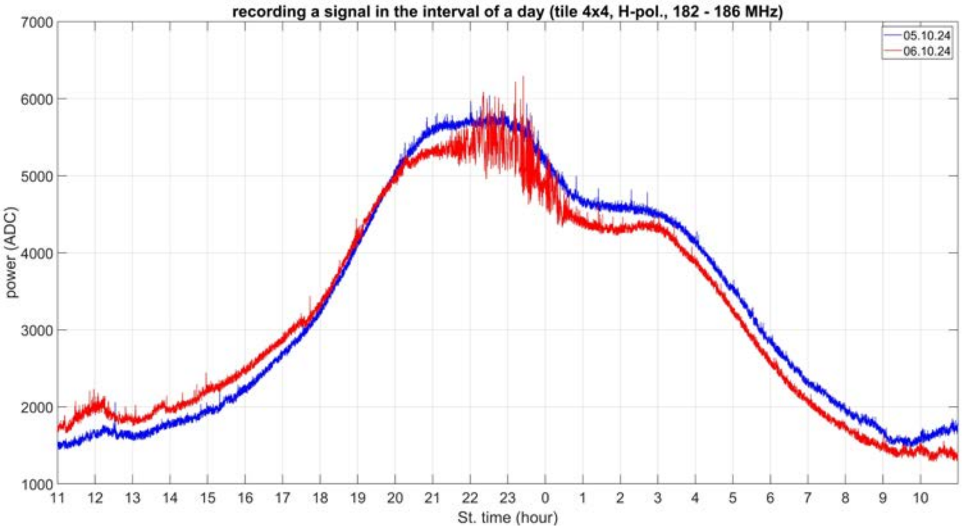

*Figure 6*. Daily recording of a signal at the output of the antenna module on October 6 and 7, 2024 (red and blue curves respectively). Ionospheric scintillation lasting about 2.5 hrs with a maximum around $23^h$ belong to source 3C 461, which has coordinates in right ascension $23^h23^m27^s$

dipoles and connected to the phasing system by coaxial cables of equal length. The same cables provide power supply to the antenna amplifiers. A metal grid with a 5×5 cm cell laid on a horizontal platform is used as the shield. The module's phasing system is housed in a closed metal box. The antenna module has been tested for more than a year because it is necessary to assess the module's performance and operational stability under various atmospheric conditions, including snow cover.

*Observations*

A total power radiometer operating in the 4 MHz band at a receiving frequency of 184 MHz was utilized as a transceiver for the antenna module. Since the beam angular size is ~20° and the effective area of the module is ~16 $m^2$, a large number of sources are covered by the antenna pattern, including the galactic plane. It is impossible to identify a separate source against this background. The strongest radio sources 3C 405 (Cygnus A) and 3C 461 (Cassiopeia A) become indistinguishable against the background of the signal from the galactic plane. Figure 6 presents two consecutive daily records. The position of the beam in the sky is fixed; therefore, the system acts as a regular meridian instrument. At ~$23^h23^m$, frequent oscillations are visible on the record for October 6, 2024 (red curve). On that day, according to radio telescope LPA data, a strong ionospheric storm occurred. Apparent oscillations are ionospheric scintillation of Cassiopeia, which makes it possible to identify this source and estimate the module's antenna beamwidth.

The antenna beamwidth of the 4×4 antenna module measured in this case from source 3C 461 at half power at a frequency of 184 MHz is 21°±1°, which is in good agreement with the calculated value.

An important practical problem in studying the characteristics of the prototype is to determine the effect of precipitation and snow cover on the operation of the antenna module, since the antennas are located at a height of 35 cm from the Earth surface and it is impossible to protect them against atmospheric precipitation. Unfortunately, the winter 2024–2025 turned out to have little snow, and Figure 5 shows the maximum snow cover. The snow-cover height is ~15 cm, lower angles of bowtie dipoles are in the snow. The waveform within 24 hours did not change in comparison with recordings without snow cover; we did not see the effect of snow on the antenna module during the winter. Since the permittivity of dry snow cover ε=1.1, which differs little from air, this result is quite explicable. There was no noticeable effect of rain on the module either. The output signal level is significantly affected by changes in ambient temperature. Temperature changes in the antenna amplifier gain cause a change in the signal level to 1 dB, depending on the amount of temperature change (the temperature coefficient is ~0.02 dB/deg.).

*Receiving system and correlator*

In this paper, we have examined the antenna part of the radio telescope, which determines its main capabilities. Along with this part, there is a receiving system designed for signal digitization and a correlator of signals coming from different modules. Signal digitization and correlation are standard procedures that have been implemented many times in different versions (see, e.g., [van Haarlem et al., 2013; Tingay et al., 2013]), in particular at the Astro Space Center of LPI RAS [Likhachev et al., 2017], which is the parent organization of PRAO. These questions concerning the antenna we propose are supposed to be addressed in a separate paper. In this paper, we do not discuss them, but we note below which points should be considered when putting the radio telescope into action.

The receiving system of the radio telescope must meet the following requirements:

- filtering, setting the signal level in channels (analog part);
- signal digitization (12-bit ADC with a sampling rate higher than 500 MHz);
- operation of all digital receivers from a single reference frequency source and their time synchronization;

- when processing a signal, a polyphase filter is employed to desample and form a signal recording band to 32 MHz with interference suppression, bit reduction up to 8 bits (the low-order bits write noise and can be eliminated);
- transmitting the digitized signal with a rate up to 640 Mb/s in one polarization from a separate module to the correlator buffer;
- buffering data from 128 receiving channels with a rate up to 640 Mb/s in the channel at the correlator input;
- real-time correlation. The number of antenna array beams generated at a time is at least 20, which is equivalent to 20 simultaneously operating correlators. The typical source tracking time is from 15 to 30 min. The correlator is supposed to be software and is developed around graphics accelerators (GPU).

The general block diagram of the radio telescope is presented in Figure 7. The radio telescope consists of 64 4×4 antenna modules providing a PAA effective area of 1000 $\mathrm{m}^2$ at a frequency of 180 MHz. Each module provides reception in two orthogonal linear polarizations.

A signal is received, digitized, and preprocessed by sixteen 8-channel digital receivers. The digital receivers are synchronized by the unified system of reference frequencies and time. The digitized signal is transmitted via fiber-optic communication lines to the main calculation server that provides signal correlation, real-time generation of at least 20 independent beams for the observed sources, and their tracking for at least 15 min.

The configuration of antenna modules for monitoring scintillating sources calls for an angular resolution of at least 20′ (no worse than that of the LPI radio telescope LPA), while there is no task of mapping the zone of observation. In this case, the most optimal from the point of view of minimizing the cost of communication lines and rooms for receiving equipment will be to mount the antenna modules at vertices of an equilateral triangle with a side 400–500 m (providing 11′–14′ angular resolution at 180 MHz). If it is necessary to expand the range of problems, the radio telescope antenna can be supplemented with modules for more uniform filling of the aperture and better coverage of the UV plane of the observed area of the sky.

## OTHER TASKS FOR THE NEW ANTENNA

Observations related to space weather forecasting are carried out during the daytime. Nighttime can be used for other tasks. Let us examine the problem of searching and studying pulsars and transients in close detail, and also briefly describe other scientific problems that can be solved with the radio telescope. It is planned to employ only 20 beams for forecasting. Nonetheless, provided that raw data is stored after the daytime session, it is possible to draw maps containing 3500 beams in a 20°×20° area if the angular resolution of the system is 20', and 14500 beams if the angular resolution of the system is 10'.

According to the section “Requirements for the new radio telescope”, for the 15 min observation interval in the 15 MHz band, ~260 mJy sensitivity at 180 MHz is provided. Given that the desired point sampling time is about 1 ms for observing pulsars and transients, the sensitivity can be determined for observations of a typical slow pulsar with a period of 0.5 s. The instantaneous sensitivity will be 4.7 Jy at $S/N=1$ and 28 Jy at $S/N=6$. By synchronously summing all pulses with a known pulsar period on the 15 min interval and with a pulsar pulse duration of 10 % of the period, the sensitivity will improve to ~0.22 Jy (at $S/N=6$).

By observing areas under the Space Weather program on a day-to-day basis and accumulating a signal over a year, with incoherent summation of the signal $S/N$ can be improved $365^{1/2}=19$ times, which will allow us to search for pulsars with ~11 mJy flux densities and conduct their long-term study. During specially organized observations lasting 8 hours at night, pulsars with an integral flux density of 2 mJy can be detected, which is comparable to the sensitivity of LOFAR.

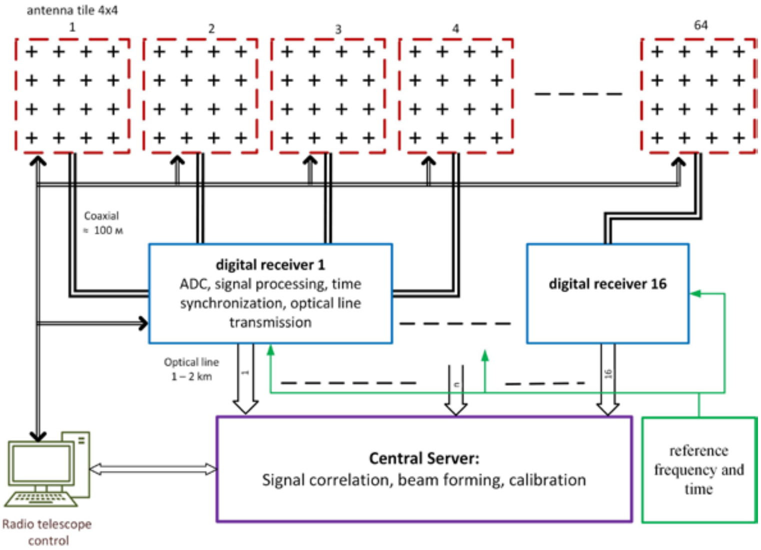

*Figure 7*. Block diagram of a radio telescope for monitoring the interplanetary plasma

In addition to searching for new pulsars, previously discovered pulsars will be observed every day. We can carry out their polarization studies, long-term observations, which allow us to separate the internal (intrinsic) and external (due to the interstellar medium) variability, to do timing of pulsars for which it has not yet been done, to look for glitches, etc.

Over the past two years, more than ten so-called long-period transients (LPT) have been discovered. Periods of these transients range from 7 min to 6.45 hrs, and the pulse duration varies from tens of seconds to ten minutes [Dong et al., 2025; Lee et al., 2025]. The nature of LPT is unknown. The main proposed search method is to draw maps for different time intervals, and then their examination and search for sources that appeared from nowhere [de Ruiter et al., 2024]. Daily observations of the sky will make it possible to detect all sources whose flux densities may be fractions of Jy.

Along with pulsars and transients, the telescope's field of view covers at least 200 scintillating radio sources in each observed area, i.e. approximately from 2000 to 4000 sources every day if we observe 9–18 areas per day (see the next section). Light curves for several years will allow us to see scintillation of sources in interstellar plasma and to reconstruct the distribution of plasma on the line of sight with high accuracy at 2–4 sq. deg. angular resolution over the celestial sphere [Tyul'bashev et al., 2019].

The observations are made in the 15 MHz band, which can shift from 120 to 240 MHz. If raw data is stored, we can form arbitrarily narrow frequency channels and observe spectral lines having different origins. These lines can also be accumulated over long-term periods.

## DISCUSSION

The module's field of view is ~20°×20°. Observations should be carried out at elongations greater than ±25°, i.e. central 50° of the front (part of the ring structure of CME) going toward us is not seen in scintillation. However, if an ejection goes directly toward us, the same changes in the scintillation index should be observed beyond elongations ±25°. Recall that scintillating sources with flux density fluctuations of 0.065 Jy at $S/N$=12 will be found at the zenith and in the center of the antenna pattern.

At the elongations, it is necessary to cover areas located between 25° and 90°. The recording time is 15 min. The front width and depth to be covered are 20°. It is, therefore, necessary to observe nine areas. Examination of these areas will take ~2 hrs.

If an ejection is detected inside the examined area, we should observe the area, located mirror symmetricaly to the meridian passing through the Sun, relative to the area with the ejection. Such observations will record scintillation indices on both sides of the Sun and give the exact direction of CME propagation relative to the Sun—Earth line [Glyantsev et al., 2014]. Alternating the two areas, where the ejection should occur, we will determine its speed. So, at the 1000 km/s speed, the ejection will travel a distance of 1 AU (or at elongations from 0° to 90°) for ~41.7 hrs (or ∼2° at elongations per hour). After detecting the ejection, we can switch every half hour (15 min to areas on different sides of the Sun) to the expected location of the ejection and very accurately assess the speed of its propagation. For a typical ejection with a speed 800–1000 km/s, we can estimate the propagation speed 5–6 times during two days of observations. Currently, it is possible to measure the CME speed from LPA observations 1–2 times during its passage, i.e. during 2–3 days. Since we can estimate the speed several times a day, the accuracy of estimating the time of CME arrival at Earth is expected to be better than that from LPA observations (now the typical accuracy is 1–3 hrs [Glyantsev et al., 2015]). The expected accuracy of predicting the CME arrival with the new antenna is at least one hour.

On the other hand, new CMEs cannot be excluded to occur. The best way is, therefore, to conduct observations 2–3 times a day (time expenditure is 1–1.5 hr) until an ejection is detected, and then to spend the remaining time searching for possible new CMEs. The proposed approach allows us to make a forecast several times a day.

For space weather forecasting, we have explored a version of the radio telescope, which consists of 64 antenna modules or 1024 base antenna elements. What will change if there are 32 or 128 modules? Since the effective area is directly proportional to the number of modules, the instantaneous sensitivity of the antenna will decrease/increase twofold.

First, take another look at the 64-module radio telescope version. As noted above in this section, sources with $\Delta S$=0.26 Jy can be easily detected when observed at angles close to the horizon and at the edge of the antenna pattern. This corresponds to $\Delta S \geq 0.4$ Jy at 102.5 MHz. According to [Artyukh et al., 1998], in a 450 sq. deg. area there are 214 scintillating radio sources. Accordingly, one source covers 2.0 sq. deg. There should be an average of 190 sources with such flux densities in the module's field of view (400 sq. deg.). Observations are planned in 20 beams, so we need to select 20 of these 190 sources, which we will observe at the selected area.

When realizing the radio telescope consisting of 32 modules, to compensate for the decreased sensitivity, it is necessary to increase the observation time fourfold, i.e. instead of 15 mins, one hour will need to scan one area. It will take nine hours to survey nine areas All other conditions being equal, forecasting will be possible once a day. There will be no time left to survey areas located at elongations on the other side of the Sun when assessing the symmetry of an ejection relative to the Sun—Earth line. At best, the speed will be estimated from two points. Tracking new CMEs becomes impossible.

The only reasonable compensation for the sensitivity degradation is to use the 32-module system to observe twice as strong sources as with the 64-module system ($\Delta S \geq 0.8$ Jy at 102.5 MHz). According to [Artyukh et al., 1998], in the 450 sq. deg. area there are 89 scintillating sources with the scintillating component flux density higher than 0.8 Jy. Hence, 1 source covers 5 sq. deg. There should be an average of 79 sources with such flux densities in the module's field of view (400 sq. deg.).

The forecasting task is still feasible, but in view of the typical depth of the front it is at the limit of the instrument's capabilities. The search for CMEs can be carried out, yet without guarantee. The main advantage of this antenna version is a fourfold reduction in the count time when searching through phase delays. The set of scientific problems that can be solved with such a radio telescope will become very limited.

For a 128-module telescope, a twofold increase in the instantaneous sensitivity makes it possible to reduce the observation time of one area fourfold, i.e. it will take 4 min to scan one area. It will take about one hour to comprehensively survey 18 areas, 9 areas on each side of the Sun (at $\Delta S$=0.26 Jy). By conducting hourly observations of an area of total size 400×18=7200 sq. deg., we can also provide a short-term forecast every hour. With the 128-module telescope, it will be possible to track CME along the entire length of the front, and not just its earthward part. At present, there is almost no detailed (quasi-simultaneous throughout the front) study of CMEs observed by the interplanetary scintillation method. The technical capability of tracking CMEs in detail will contribute to a better understanding of both the structure of CMEs and the characteristics of their distribution in the interplanetary medium. This radio telescope version is, therefore, much preferable to the 64-module one. However, the count time will increase fourfold in searching for phase delays.

Along with CMEs, corotating structures are also known, which can also cause magnetic storms. The intensity of such storms is low compared to that of CME-driven storms. According to LPA observations [Chashei et al., 2023], corotating structures are usually observed 2–3 days before their arrival at Earth in the form of a decrease in the scintillation index ahead of the corotating structure front and are easy to detect.

We have examined an ideal forecasting scheme that ignores the realities on the earth. For example, thunderstorms or power grid failures will lead to the fact that a space weather forecast cannot be given. A 1500 km/s fast ejection at night cannot be tracked. Regular routine maintenance, which can take several days, is carried out on telescopes. Therefore, a service that provides space weather forecasts must have several radio telescopes located at different longitudes. Switching-off one or two telescopes, no matter for what reason, will allow the remaining telescopes to monitor CMEs.

## CONCLUSION

Comparing the scintillation index of interplanetary compact radio sources under quiet and excited solar wind conditions allows us to estimate the speed and direction of CME propagation, as well as to detect corotating structures. It is shown that a radio telescope with a wide field of view and the capability of making repetitive observations of the same sources is necessary for monitoring scintillating sources.

To solve the applied problem of predicting geomagnetic storms, a radio telescope project based on the phased array antenna operating in the 120–240 MHz range has been proposed for monitoring interplanetary plasma. It is demonstrated that besides the applied problem — space weather forecasting — scientific problems can be solved with the aid of such a telescope.

The ideal antenna for space weather forecasting is a 128-module device that can produce forecasts at least 4–6 times a day, as well as track possible repeated CMEs. Forecasting can easily be done with a 64-module telescope, but with very little time to search for new CMEs that may occur on the same days as the monitored ejection. Forecasting with a 32-module telescope is still possible, but there is no enough time, it is almost impossible to monitor repeated CMEs, and the forecast will most likely be made once a day.

We have substantiated technical requirements for the radio telescope, determine its structural configuration, and requirements for functional elements.

Further scaling of the radio telescope is possible, including the deployment of its elements in other regions of the Russian Federation, which will improve the accuracy and reliability of the forecast.

The work was carried out under the Government assignment. We thank I.V. Chashei for the preliminary reading of the manuscript and useful comments, as well as L.B. Potapov for his assistance in preparing the paper and Figures.

## REFERENCES

Artyukh V.S., Tyul'bashev S.A. A method for analyzing a survey of scintillating radio sources. *Astronomy Reps*. 1996a, vol. 40, iss. 5, pp. 608–615.

Artyukh V.S., Tyul'bashev S.A. The cosmological evolution of compact radio sources from 102 MHz observations. *Astronomy Rep*. 1996b, vol. 40, iss. 5, pp. 601–607.

Artyukh V.A., Tyul'bashev S.A., Isaev E.A. The cosmological evolution of compact radio sources from 102-MHz observations. *Astronomy Rep*. 1998, vol. 42, iss. 3, pp. 576–586.

Bisi M.M., Breen A.R., Jackson B.V., et al. From the Sun to the Earth: The 13 May 2005 coronal mass ejection. *Solar Phys*. 2010, vol. 265, iss. 1-2, pp. 49–127. https://doi.org/10.1007/s11207-010-9602-8.

Bisi M.M., Fallows, R.A., Jackson, B.V., et al. The Worldwide Interplanetary Scintillation (IPS) Stations (WIPSS) Network October 2016 Observing Campaign: Initial WIPSS Data Analyses. *AGU Fall Meeting Abstracts*. 2017, SH21A-2648.

Chashei I.V., Tyul'bashev S.A., Subaev I.A., Izvekova V.A. Global structure of the solar wind in a of decreasing solar activity from interplanetary-scintillation monitoring data. *Astronomy Rep*. 2019, vol. 63, iss. 2, pp. 161–165. https://doi.org/10.1134/S1063772919020021.

Chashei I.V., Tyul'bashev S.A., Lukmanov V.R., Subaev I.A. ICMEs and CIRs monitored in IPS data at a frequency of 111 MHz. *Adv. Space Res*. 2023, vol. 72, iss. 12, pp. 5371–5375. https://doi.org/10.1016/j.asr.2022.05.050.

Chen P.F. Coronal mass ejections: Models and their observational basis. *Living Rev. Sol. Phys.* 2011, vol. 8, iss. 1, pp.1–92. https://doi.org/10.12942/lrsp-2011-1.

Dagkesamanskii R.D., Veselovskii A.V., Zheleznykh I.M., et al. Prototype of a Meter-Wavelength Radio Telescope with wide field-of-view. *Bull. Lebedev Physics Institute*. 2020, vol. 47, iss. 3, pp. 71–75. https://doi.org/10.3103/S1068335620030021.

de Ruite I., Meyers Z.S., Rowlinson A., et al. Transient study using LoTSS - framework development and preliminary results. *Mont. Not. Roy. Astron. Soc*. 2024, vol. 531, iss. 4, pp. 4805–4822. https://doi.org/10.1093/mnras/stae1458.

Dong F.A., Clarke T.E., Curtin A., et al. CHIME/fast radio burst/pulsar discovery of a nearby long-period radio transient with a timing glitch. *Astrophys. J. Lett.* 2025, vol. 990, iss. 2, pp. L49–L64. https://doi.org/10.3847/2041-8213/adfa8e.

Fallows R.A., Iwai K., Jackson B.V., et al. Application of novel interplanetary scintillation visualisations using LOFAR: A case study of merged CMEs from September 2017. *Adv. Space Res.* 2023, vol. 72, iss. 12, pp. 5311–5327. https://doi.org/10.1016/j.asr.2022.08.076.

Ghuge D., Bhattacharjee D., Subramanian P. Turbulent power: A discriminator between sheaths and CMEs. *Solar Phys.* 2025, vol. 300, iss. 4, id. 47. https://doi.org/10.1007/s11207-025-02457-5.

Glubokova S.K., Tyul’bashev S.A., Chashei I.V., Shishov V.I. Parameters of the turbulence of the interplanetary plasma derived from scintillation observations of the quasar 3C 48 at the solar-activity minimum. *Astronomy Rep*. 2013, vol. 57, iss. 8, pp. 586–593. https://doi.org/10.1134/S1063772913070020.

Glyantsev A.V., Tyul’bashev S.A., Chashei I.V., Shishov V.I. The detection of coronal mass ejections in the interplanetary medium using scintillation observations. *Astronomy Rep*. 2014, vol. 58, iss. 9, pp. 619–625. https://doi.org/10.1134/S1063772914090030.

Glyantsev A.V., Tyul’bashev S.A., Chashei I.V., Shishov V.I. Interplanetary-scintillation observations of coronal mass ejections near the maximum of the 24th solar-activity cycle. *Astronomy Rep*. 2015, vol. 59, iss. 1, pp. 40–45. https://doi.org/10.1134/S1063772915010047.

Goncharenko I.V. *Computer simulation of antennas. All about the MMANA program*. Moscow, RadioSoft Publ., 2002, 80 p. (In Russian).

Gosling J.T., Hildner E., MacQueen R.M., et al. Mass ejections from the Sun: A view from Skylab. *J. Geophys. Res*. 1974, vol. 79, iss. 31, pp. 4581–4587. https://doi.org/10.1029/JA079i031p04581.

Gosling J.T., Hildner E., MacQueen R.M., et al. The speeds of coronal mass ejection events. *Solar Phys*. 1976, vol. 48, iss. 2, pp. 389–397. https://doi.org/10.1007/BF00152004.

Hewish A., Scott P.F., Wills D. Interplanetary scintillation of small diameter radio sources. *Nature*. 1964, vol. 203, iss. 4951, pp. 1214–1217. https://doi.org/10.1038/2031214a0.

Hewish A., Dennison P.A., Pilkington J.D.H. Measurements of the size and motion of the irregularities in the interplanetary medium. *Nature*. 1966, vol. 209, iss. 5029, pp. 1188–1189. https://doi.org/10.1038/2091188a0.

Iwai K., Shiota D., Tokumaru M., et al. Development of a coronal mass ejection arrival time forecasting system using interplanetary scintillation observations. *Earth, Planets and Space*. 2019, vol. 71, iss. 1, 39. https://doi.org/10.1186/s40623-019-1019-5.

Kojima M., Tokumaru M., Watanabe H., et al. Heliospheric tomography using interplanetary scintillation observations 2. Latitude and heliocentric distance dependence of solar wind structure at 0.1-1 AU. *J. Geophys. Res.* 1998, vol. 103, A2, pp. 1981–1990. https://doi.org/10.1029/97JA02162.

Lee Y.W.J., Caleb M., Murphy T., et al. The emission of interpulses by a 6.45-h-period coherent radio transient. *Nature Astronomy*. 2025, vol. 9, pp. 393–405. https://doi.org/10.1038/s41550-024-02452-z.

Likhachev S.F., Kostenko V.I., Girin I.A., et al. Software Correlator for Radioastron Mission. *Journal of Astronomical Instrumentation*. 2017, vol. 6, iss. 3, id 1750004-131. https://doi.org/10.1142/S2251171717500040.

Lukmanov V.R., Chashei I.V., Tyul’bashev S.A. On correlation of the interplanetary scintillation level and solar wind speed. *Astronomy Rep.* 2022, vol. 66, iss. 12, pp. 1325–1328. https://doi.org/10.1134/S1063772922110142.

Manoharan P.K., Ananthakrishnan S., Dryer M., et al. Solar wind velocity and normalized scintillation index from single-station IPS observations. *Solar Phys.* 1995, vol. 156, iss. 2, pp. 377–393. https://doi.org/10.1007/BF0067023.

Manoharan P.K., Tokumaru M., Pick M., et al. Coronal mass ejection of 2000 July 14 flare event: Imaging from near-Sun to Earth environment. *Astrophys. J.* 2001, vol. 559, iss. 2, pp. 1180–1189. https://doi.org/10.1086/322332.

Marians M. Computed scintillation spectra for strong turbulence. *Radio Sci*. 1975, vol. 10, pp. 115–119. https://doi.org/10.1029/RS010i001p00115.

Mejia-Ambriz J.C., Jackson B.V., Gonzalez-Esparza J.A., et al. Remote-sensing of solar wind speeds from IPS observations at 140 and 327 MHz using MEXART and STEL. *Solar Phys*. 2015, vol. 290, iss. 9, pp. 2539–2552. https://doi.org/10.1007/s11207-015-0694-z.

Millward G., Biesecker D., Pizzo V., de Koning C.A. An operational software tool for the analysis of coronagraph images: Determining CME parameters for input into the WSA-Enlil heliospheric model. *Space Weather*. 2013, vol. 11, iss. 2, pp. 57–68. https://doi.org/10.1002/swe.20024.

Morgan J., McCauley P.I., Waszewski A., et al. Detection and characterization of a coronal mass ejection using interplanetary scintillation measurements from the Murchison Widefield Array. *Space Weather*. 2023, vol. 21, iss. 5, e2022SW003396. https://doi.org/10.1029/2022SW003396.

Petrukovich A.A. Solar-terrestrial relations and space weather. *Plasma Heliogeophysics*. Moscow, Nauka Publ., 2008, pp. 175–257. (In Russian).

Readhead A.C.S. Interplanetary scintillation of radio sources at metre wave-lengths-II. Theory. *Mont. Not. Roy. Astron. Soc*. 1971, vol. 155, p. 185. https://doi.org/10.1093/mnras/155.2.185.

Romero-Hernandez E., Gonzalez-Esparza J.A., Aguilar-Rodriguez E., et al. detection of solar wind disturbances: Mexican Array Radio Telescope IPS observations at 140 MHz. *Solar Phys*. 2015, vol. 290, iss. 9, pp. 2553–2566. https://doi.org/10.1007/s11207-015-0690-3.

*Antenna Toolbox – MATLAB*, 2023. Available at: https://www.mathworks.com/products/antenna.html (accessed December 12, 2025).

Tingay S.J., Goeke R., Bowman J.D., et al. The Murchison Widefield Array: The square kilometre array precursor at low radio frequencies. *Publ. Astron. Soc. Australia*. 2013, vol. 30, e007, 21 p. https://doi.org/10.1017/pasa.2012.007.

Tokumaru M., Kojima M., Fujiki K. Solar cycle evolution of the solar wind speed distribution from 1985 to 2008. *J. Geophys. Res.: Space Phys*. 2010, vol. 115, iss. A4, CiteID A04102. https://doi.org/10.1029/2009JA014628.

Tokumaru M., Kojima M., Fujiki K. Long-term evolution in the global distribution of solar wind speed and density fluctuations during 1997–2009. *J. Geophys. Res.: Space Phys*. 2012, vol. 117, iss. A6, A06108. https://doi.org/10.1029/2011JA017379.

Tyul’bashev S.A., Golysheva P.Y., Tyul’bashev V.S., Subaev I.A. Search for long-term variability of several flat-spectrum sources at 111 MHz. *Astronomy Reports*. 2019, vol. 63, iss. 11, pp. 920–931. https://doi.org/10.1134/S1063772919100068.

Turtle A.J., Baldwin J.E. A survey of galactic radiation at 178 Mc/s. *Mont. Not. Roy. Astron. Soc*. 1962, vol. 124, p. 459. https://doi.org/10.1093/mnras/124.6.459.

Shishov V.I., Chashei I.V., Oreshko V.V., et al. Monitoring of the turbulent solar wind with the upgraded Large Phased Array of the Lebedev Institute of Physics: First results. *Astronomy Reports*. 2016, vol. 60, iss. 12, pp. 1067–1082. https://doi.org/10.1134/S1063772916110068.

van Haarlem M.P., Wise M.W., Gunst A.W., et al. LOFAR: The LOw-Frequency Array. *Astron. Astrophys*. 2013, vol. 556, A2, 53 p. https://doi.org/10.1051/0004-6361/201220873.

Vlasov V.I. Solar-wind velocity measurement by radio observations of phenomena propagated through the interplanetary plasma. *Soviet Astronomy Letters*. 1979, vol. 5, pp. 154–156.

Vlasov V.I., Chashei I.V., Shishov V.I., Shishova T.D. Interplanetary plasma from radioastronomical data (Review). *Geomagnetism and Aeronomy*. 1979, vol. 19, pp. 269–282.

Voskresenskii D.I. *Microwave devices and Antennas (Design of phased array antennas)*. Moscow, Radio i Svyaz' Publ., 1981, 432 p. (In Russian).

Wagner W.J. SERF studies of mass motions arising in flares. *Adv. Space Res*. 1982, vol. 2, iss. 11, pp. 203–219. https://doi.org/10.1016/0273-1177(82)90201-0.

Wang Y.M., Sheeley N.R., Socker D.G., et al. Observations of correlated white-light and extreme-ultraviolet jets from polar coronal holes. *Astrophys. J*. 1998, vol. 508, iss. 2, pp. 899–907. https://doi.org/10.1086/306450.

Waszewski A., Morgan J.S., Chhetri R., et al. Resolving moving heliospheric structures using interplanetary scintillation observations with the Murchison Widefield Array. *Space Weather*. 2023, vol. 21, iss. 10, e2023SW003570. https://doi.org/10.1029/2023SW003570.

Yashiro S., Gopalswamy N., Michalek G., et al. A catalog of white light coronal mass ejections observed by the SOHO spacecraft. *J. Geophys. Res.: Space Phys*. 2004, vol. 109, iss. A7, A07105. https://doi.org/10.1029/2003JA010282.

URL: http://spaceweather.izmiran.ru/ (accessed December 12, 2025).

URL: https://iszf.irk.ru/megascience/ (accessed December 12, 2025).

URL: http://ipg.geospace.ru/space-weather-forecast.html (accessed December 12, 2025).

URL: www.swpc.noaa.gov (accessed December 12, 2025).

URL: wdc.kugi.kyoto-u.ac.jp (accessed December 12, 2025).

URL: http://www.cessi.in/spaceweather/ (accessed December 12, 2025).

URL: https://swe.ssa.esa.int/ (accessed December 12, 2025).

URL: http://www.spaceweather.org/ISES/rwc/rwc_cn_a.html (accessed December 12, 2025).

URL: https://ccmc.gsfc.nasa.gov/models/WSA-Enlil-at-SWPC~3/ (accessed December 12, 2025).

URL: https://www.ncei.noaa.gov/ (accessed December 12, 2025).

URL: https://www.nesdis.noaa.gov/current-satellite-missions/currently-flying/dscovr-deep-space-climate-observatory (accessed December 12, 2025).

URL: https://www.swpc.noaa.gov/products/ace-real-time-solar-wind (accessed December 12, 2025).

URL: https://www.mathworks.com/products/antenna.html (accessed December 12, 2025).

URL: https://sw.prao.ru/ (accessed December 12, 2025).

Original Russian version: Oreshko V.V., Tyul'bashev S.A., published in Solnechno-zemnaya fizika. 2026, vol. 12, no. 2, pp. 105–118. https://doi.org/10.12737/szf-122202611.

*How to cite this article*

Oreshko V.V., Tyul'bashev S.A. Radio telescope for monitoring the state of interplanetary plasma. *Sol.-Terr. Phys.* 2026, vol. 12, iss. 2, pp. 96–108. https://doi.org/10.12737/stp-122202611 .